Discover Applied Sciences

RESEARCH Open Access

Naturally derived nano-ceramic composites with enhanced dielectric performance for electronics applications

Kiran Keshyagol[1], Shivashankarayya Hiremath[1*], H. M. Vishwanatha[1], Pavan Hiremath[1] and Tae-Won Kim[2]

*Correspondence:
Shivashankarayya Hiremath
ss.hiremath@manipal.edu
[1]Manipal Institute of Technology, Manipal Academy of Higher Education, Manipal, Karnataka 576104, India
[2]Department of Mechanical Engineering, Hanyang University, Seongdong-gu, Seoul 04763, Korea

Abstract

Polydimethylsiloxane (PDMS) is a widely used elastomer for flexible electronics, but its low dielectric permittivity limits charge storage and sensitivity in capacitive devices. In this study, a sustainable CaO-rich filler, Naturally Extracted Dielectric (NED)—was produced from biowaste cuttlefish bone via calcination and incorporated into PDMS to fabricate Flexible Composite Films (FCF). The PDMS and NED composite was prepared by solution casting with controlled loadings (2.5, 5, 7.5, and 10 wt.%). The structural and chemical integrity were confirmed by X-ray Diffraction (XRD) and Fourier Transform Infrared Spectroscopy (FTIR), indicating successful filler incorporation without the formation of new phases of the PDMS network. Optical analysis showed a wide band gap (~3.27–3.33 eV), consistent with dielectric behavior. Scanning Electron Microscopy (SEM) with Energy-Dispersive X-ray Spectroscopy (EDS) revealed dispersed filler domains with increasing surface roughness and mild agglomeration at 10 wt.% NED. Impedance spectroscopy showed depressed semicircles well fitted by a Bulk resistance (R_b) parallel with Constant Phase Element (CPE) model, indicating bulk-controlled, non-Debye relaxation; bulk resistance decreased to a minimum at 7.5 wt.% and slightly increased at 10 wt.% due to microstructural limitation. Dielectric spectra exhibited strong low-frequency interfacial polarization, with dielectric loss of 0.13–0.18 in of mid-frequency range. Overall, the optimized PDMS:NED composition (notably 7.5 wt.%) provides a promising flexible dielectric platform for capacitive pressure sensors and wearable electronics applications. Also, as a dielectric and tribo-layer candidate for triboelectric nanogenerators (TENGs), where permittivity and interfacial polarization are performance-relevant.

Keywords Dielectrics, Flexible composite films, Permittivity, Electrical conductivity, Naturally extracted dielectrics, Calcium oxide, Sustainable development goals

1 Introduction

Flexible and wearable electronics are rapidly expanding into human–machine interfaces, e-skin, and health-oriented monitoring, where soft sensors must remain stable under repeated bending, compression, and stretching [1–4]. Among these, capacitive pressure

© The Author(s) 2026. **Open Access** This article is licensed under a Creative Commons Attribution 4.0 International License, which permits use, sharing, adaptation, distribution and reproduction in any medium or format, as long as you give appropriate credit to the original author(s) and the source, provide a link to the Creative Commons licence, and indicate if changes were made. The images or other third party material in this article are included in the article's Creative Commons licence, unless indicated otherwise in a credit line to the material. If material is not included in the article's Creative Commons licence and your intended use is not permitted by statutory regulation or exceeds the permitted use, you will need to obtain permission directly from the copyright holder. To view a copy of this licence, visit http://creativecommons.org/licenses/by/4.0/.

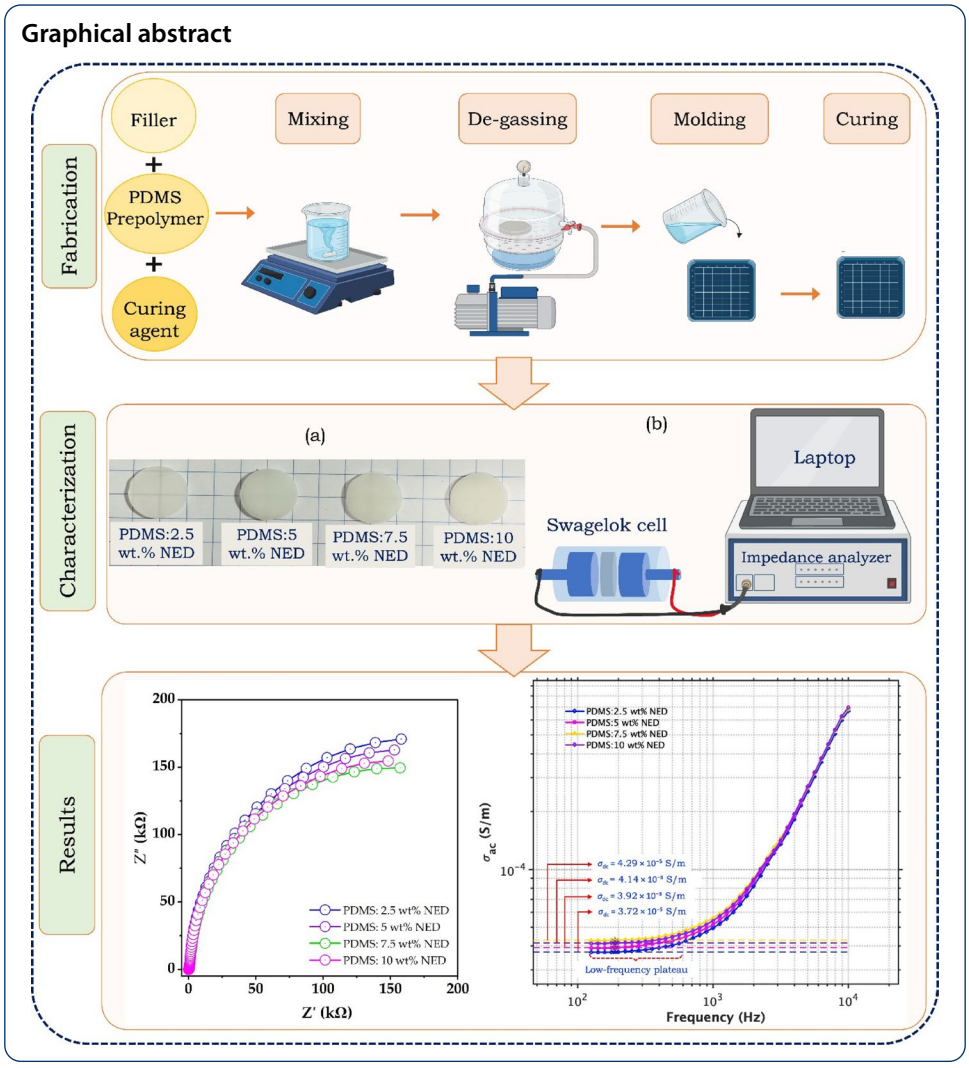

sensors (CPSs) are widely pursued because of their structural simplicity, low power consumption, and compatibility with textile/skin-integrated platforms [5, 6]. In parallel, triboelectric nanogenerators (TENGs) have become viable options for self-powered wearable sensing and mechanical energy harvesting, thus creating the need for dielectric/tribo-layer materials to support high charge density and stability under deformation [7–9]. Within this application context, the current study is instantly relevant to the following sustainable development goals (SDG) themes: (i) wearable sensing for continuous and non-invasive monitoring, which is relevant to SDG 3, "Good Health and Well-Being" [10]; and (ii) the development of functional materials through biowaste valorization, which is relevant to SDG 12, "Responsible Consumption and Production" [11]. Dielectric polymer composite materials are significant in the field of capacitive devices due to their ability to be tailored for dielectric response while retaining flexibility [12]. Polydimethylsiloxane (PDMS), in particular, is interesting as a flexible dielectric matrix material due to its electrical insulation and mechanical flexibility, as well as its ease of processing and curing. However, it is normally found to have low dielectric permittivity [13, 14]. This limitation is of particular significance for CPS structures, where the capacitance response with pressure is heavily dependent on the intermediate dielectric

layer's permittivity and compressibility [15]. Hence, the improvement of the dielectric properties of PDMS without compromising its inherent flexibility is a subject of current research. A very common approach to overcome this limitation is the incorporation of high permittivity inorganic fillers into the PDMS matrix. In recent years, PDMS composite materials with high-k value inorganic fillers such as $BaTiO_3$ [16], TiO_2 [17], ZnO [18], and $CaCu_3Ti_4O_{12}$ [19] have been widely researched for various applications in flexible electronics, capacitive sensing, and energy harvesting. These fillers are used to improve the value of the dielectric constant of the composite material using their inherent high permittivity. $BaTiO_3$/PDMS composite materials have been widely researched for various applications. $BaTiO_3$ is a classical ferroelectric ceramic material with a high value of permittivity [20]. Similarly, TiO_2 has been used as a dielectric modifier for PDMS due to its stable dielectric properties, low cost, and processability with polymers [21]. PDMS-ZnO composite dielectrics have been studied, where ZnO is expected to improve dielectric properties while providing other advantages, including semiconducting and electromechanical effects [22]. In addition, CCTO-based polymer composite dielectrics have been studied, where the dielectric constant is exceptionally high, which can improve dielectric properties significantly if good filler dispersion is achieved [23, 24]. These studies show that dielectric enhancement in PDMS composite dielectrics is not only dependent on the permittivity of the filler material, but filler loading, filler morphology, filler dispersion, and the interface between the filler and polymer play an important role in achieving improved permittivity with reduced dielectric loss. Recent studies by CPS have further emphasized that dielectric layer engineering is one of the most efficient approaches for improving the sensitivity of the sensor, keeping the structural simplicity and device manufacturability intact [10]. In this direction, the modulation of relative permittivity by filler addition has been recognized as a crucial factor for designing PDMS-based pressure sensors [25]. In the case of TENG, material engineering is also moving towards polymer composites and interface engineering for improving the dielectric properties, suppressing charge decay, and improving device stability during long periods of deformation [26]. In addition, it has been reported that microstructural engineering, such as porosity, surface roughness, and texture, can be used synergistically with dielectric engineering for improving the overall charge generation, retention, and sensing properties of the device [27, 28]. In particular, the improvement of triboelectric properties of PDMS by filler addition has been reported, thereby confirming the general understanding that a high value of effective dielectric constant can facilitate better charge accumulation and device response [29]. In contrast, Ca-based oxide materials have received relatively little attention for improving the dielectric properties of polymer composites, although they can be a cost-effective and more sustainable option for improving material properties. In particular, CaO can be extracted from naturally abundant materials such as seashells, eggshells, animal bones, cuttlebone, etc., through thermal conversion [30, 31]. Such an approach not only enables waste valorization, but also offers a pathway toward sustainable functional fillers for flexible electronic materials. Prior studies have shown that calcium-rich biogenic structures can be transformed into CaO-rich phases through calcination, including reports on cuttlebone-derived systems converted in the temperature range of approximately 700–750 °C [32, 33]. Moreover, calcium oxide and calcium-derived ceramic systems have been explored in various composite and functional materials where modifications in dielectric, electrical, or interfacial

characteristics are desired. In the earlier study, author have demonstrated that cuttlefish bone powder can be transformed from $CaCO_3$ to CaO and that the resulting material exhibits dielectric behavior dominated by Maxwell–Wagner interfacial polarization [34]. These findings suggest that bio-derived CaO-rich materials may serve as promising dielectric fillers for flexible polymer composites. Despite the progress made using conventional high-k fillers, studies involving naturally extracted CaO-rich fillers in PDMS remain very limited, particularly under systematically controlled filler concentrations and with a detailed correlation between composition, dielectric response, and impedance characteristics. This gap is scientifically important because CaO-rich fillers derived from biogenic waste could provide a sustainable alternative to conventional ceramic dielectric additives while introducing distinct interfacial polarization behavior. Hence, it is necessary to have a systematic study of PDMS: NED composites to understand the degree to which this filler may impact dielectric storage, dielectric loss, and transport.

In this work, a CaO-rich NED filler derived from cuttlefish bone is synthesized by calcination at 750 °C with a 60-min dwell time, grinding, probe sonicating, and lyophilization to obtain a fine powder ready to be incorporated into a composite material. PDMS:NED flexible composite materials are synthesized by using a solution-casting method with PDMS as the matrix and NED as the filler at 2.5, 5, 7.5, and 10 wt.%. The electrical properties of the materials are measured using Impedance Spectroscopy at Room Temperature (RT), and the dielectric properties of the materials are measured using dielectric functions such as ε', ε'', and tan δ.

2 Material and methods

2.1 Extraction of filler material from cuttlefish bone

The raw material for preparing the filler material was cuttlefish bone, and the resulting material was referred to as Naturally Extracted Dielectric (NED). The route followed for the extraction of NED from the cuttlefish bone, is illustrated in Fig. 1**.** In this process, the cuttlefish bones were subjected to heating from RT to 750 °C. After attaining the required temperature, the sample was subjected to isothermal treatment for a period of 60 min. After this treatment, the sample was cooled to RT under ambient conditions. The calcined cuttlefish bone was then powdered using a mortar and pestle and stored for further processing. To obtain a more homogeneous particle size, the powder was subjected to probe sonication for 30 min. The processed sample was subsequently frozen at −80 °C for 24 h and then placed in a freeze dryer for lyophilization for approximately 62 h to ensure complete moisture removal.

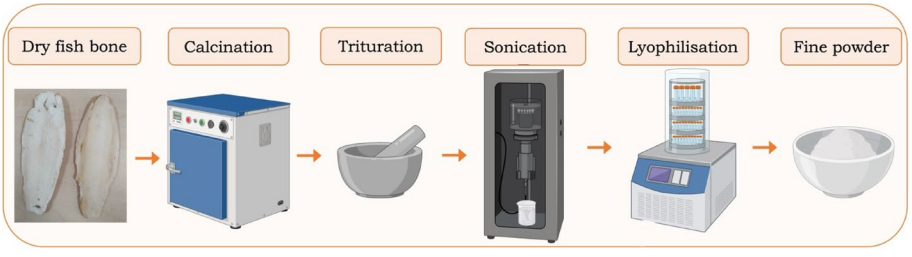

Fig. 1 Process involved in the extraction of NED from cuttlefish bone

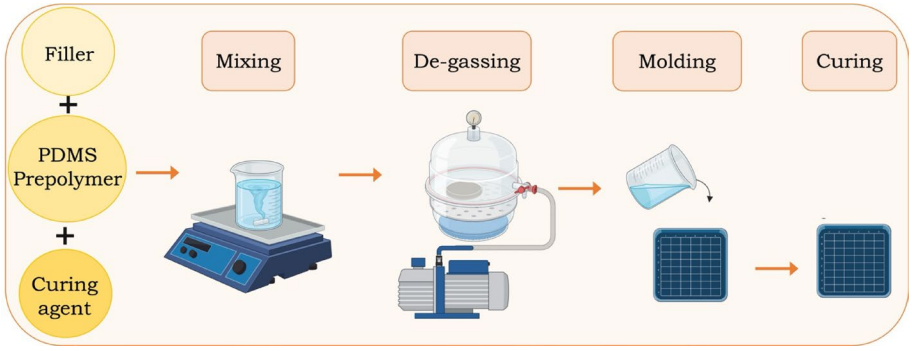

Fig. 2 Preparation of PDMS and NED composite by the solution casting method

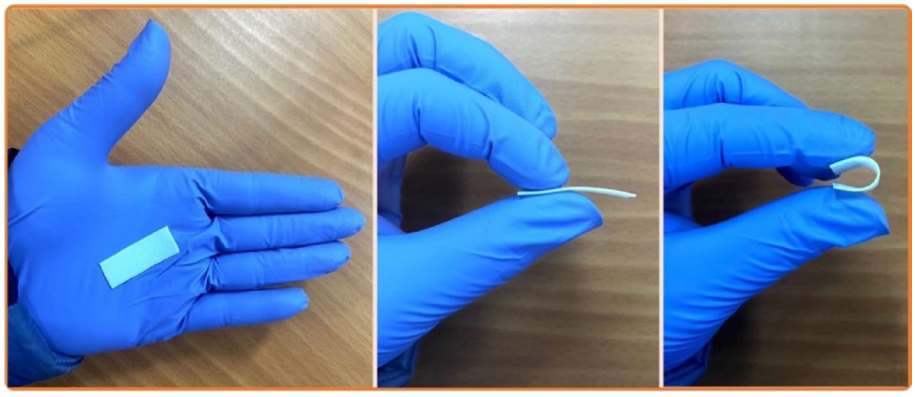

Fig. 3 Stand-alone PDMS: NED Composite samples

2.2 Fabrication of composite material

The PDMS:NED-based flexible composite film (FCF) was fabricated using the solution-casting method, as illustrated in Fig. 2. PDMS (Sylgard 184, Dow Corning) was used as the polymer matrix, and NED was incorporated into the PDMS at four different loadings, namely 2.5, 5, 7.5, and 10 wt.%, to prepare the flexible composite films. The NED powder was incorporated into the PDMS prepolymer at the required filler loading and magnetically stirred for 1 h to promote uniform dispersion of the filler within the prepolymer. Subsequently, the curing agent was added to the prepolymer filled of NED to form a PDMS at a 10:1 (prepolymer: curing agent) mass ratio and NED composite, followed by additional mixing using a magnetic stirrer and manual stirring with a glass rod to ensure complete homogenization. The resulting mixture was degassed to remove entrapped air bubbles and then poured into pre-cleaned molds. The cast samples were allowed to cure naturally at RT for 48 h. After curing, the composite films were carefully peeled from the molds (Fig. 3). The same procedure was repeated for all four compositions.

2.3 Characterization

To evaluate the composite materials, a series of characterization techniques were employed. X-ray diffraction analysis was performed using a Rigaku Miniflex 600 (5th generation) diffractometer. The diffraction data were collected over a 2θ range of 10° to 90° at a scanning rate of 2° min^{-1} with Cu Kα radiation (λ = 1.54 Å) from a copper anode source. FTIR measurements were conducted at RT using a Shimadzu IR Spirit ATR-FTIR spectrometer. The spectra were acquired in transmittance mode within the

spectral range of 500–4000 cm^{-1} at a resolution of 4 cm^{-1}. Diffuse reflectance spectroscopy was carried out using a PerkinElmer Lambda 750 s UV/Vis/NIR spectrophotometer to estimate the band gap of all samples. The surface morphology of the composite films was examined by SEM using a Carl Zeiss EVOMA-18 microscope integrated with an Oxford Instruments X-act EDS detector. Microstructural and elemental observations were obtained at magnifications of 1000 × and 30,000 ×. The electrical behavior of the FCF samples was studied using an OrigaFlex electrochemical workstation. Each sample was shaped into a circular pellet of 24 mm diameter and approximately 1 mm thickness, as shown in Fig. 4a**.** The pellet was mounted inside a Swagelok cell connected to the impedance analyzer, as depicted in Fig. 4b. Impedance analysis was performed at RT over the frequency range of 100 Hz–10 kHz under an AC excitation of 2 V. The instrument was computer interfaced for automatic acquisition and processing of the data, from which the real (Z′) and imaginary (Z″) parts of the complex impedance (Z*) were obtained.

Once the complex impedance Z^* data were obtained, additional dielectric and electrical parameters were calculated. In particular, the complex permittivity (ε^*) and complex electric modulus (M^*) were evaluated based on the relationships given in [35]. A brief summary of the theoretical formulation is provided below.

$$Z^* = Z\prime - jZ'' \tag{1}$$

$$\varepsilon^* = \frac{1}{j\omega C_0 Z^*} = \varepsilon\prime - j\varepsilon'' \tag{2}$$

$$M^* = \frac{1}{\varepsilon^*} = j\omega C_0 Z^* = M\prime + jM'' \tag{3}$$

From these, the real and imaginary parts of permittivity are derived as:

$$\varepsilon\prime = \frac{Z''}{\omega C_0 \left(Z'^2 + Z''^2\right)} \tag{4}$$

$$\varepsilon'' = \frac{Z\prime}{\omega C_0 \left(Z'^2 + Z''^2\right)} \tag{5}$$

In the above equations, $C_0 = \frac{\varepsilon_0 A}{t}$ denotes the vacuum capacitance, where ε_0 is the permittivity of free space, A refers to the electrode area, and t is the sample thickness. The

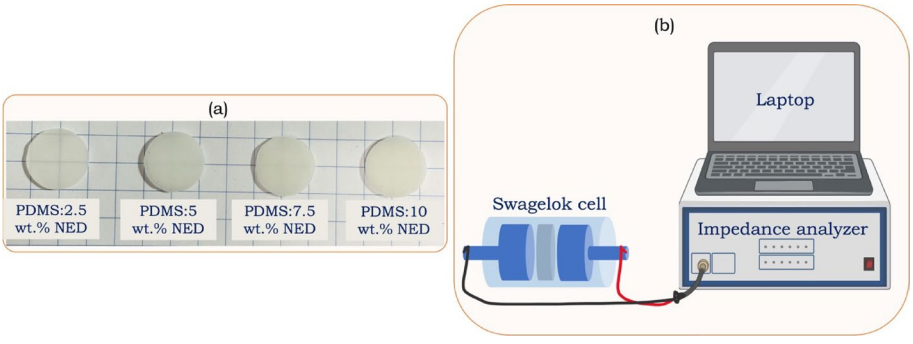

Fig. 4 **a** PDMS and NED composite pellets used for the experiment, **b** Impedance analyzer setup

angular frequency is given by $\omega = 2\pi f$, with f representing the applied AC frequency. The dielectric loss tangent is defined by Eq. (6).

$$\tan\delta = \frac{\varepsilon''}{\varepsilon'} \tag{6}$$

Similarly, the real and imaginary components of the electric modulus are calculated as given in Eqs. (7) and (8).

$$M' = \frac{\varepsilon'}{\varepsilon'^2 + \varepsilon''^2} = \omega C_0 Z'' \tag{7}$$

$$M'' = \frac{\varepsilon''}{\varepsilon'^2 + \varepsilon''^2} = \omega C_0 Z' \tag{8}$$

The AC conductivity was computed using Eq. (9)

$$\sigma_{\mathrm{ac}} = \frac{Z_r}{Z_r^2 + Z_i^2} \cdot \frac{t}{A} \tag{9}$$

$$\sigma_{ac}(\omega) = \sigma_{dc} + A\omega^s \quad with \quad 0 < s < 1 \tag{10}$$

As mentioned in Eq. (10), the ion transport is explained by a hopping model, where A stands for the temperature-dependent constant, and s is the characteristic frequency exponent [36]. The additional term is used to explain the interfacial charge accumulation and dipole polarization, which increase with increasing frequency [36]. In this manner, $\sigma_{ac}(\omega)$ can be regarded as a measure of the ionic interaction level and the charge transfer mechanism. The R_b value of the impedance plot [37], where the Z′ axis is intersected, was used to obtain the ionic conductivity of NED at RT according to Eq. (11) [38].

$$\sigma_{dc} = \frac{t}{R_b A} \tag{11}$$

3 Results and discussion

3.1 Structural and chemical analyses

The XRD analysis was performed for pure PDMS, NED-750 powder, and PDMS:NED composite films with 2.5, 5, 7.5, and 10 wt.% filler loading, as shown in Fig. 5. As reported in previous study [34], the XRD pattern of the NED-750 sample was indexed to the cubic CaO phase (space group Fm-3 m), confirming the successful thermal conversion of the precursor into calcium oxide at 750 °C. The NED-750 powder exhibited distinct diffraction peaks at 2θ are 32.256°, 37.408°, 53.981°, 64.285°, and 67.583°, which match well with JCPDS-48–1467, thereby confirming the crystalline CaO phase. The same diffraction peaks were also observed in all PDMS:NED composites, indicating the successful incorporation of NED-750 into the PDMS matrix. Pure PDMS showed a broad diffraction peak centered at 12.85°, which is characteristic of its predominantly amorphous structure. In addition to the major peaks, some minor peaks were also observed in the composite patterns, and these are indicated by an asterisk (*).

Figure 6a presents the chemical structure of PDMS, while Fig. 6b shows the FTIR spectra of the PDMS:NED composite films containing 2.5, 5, 7.5, and 10 wt.% NED. In Fig. 6b, all composite films exhibit the typical absorption bands of PDMS, confirming

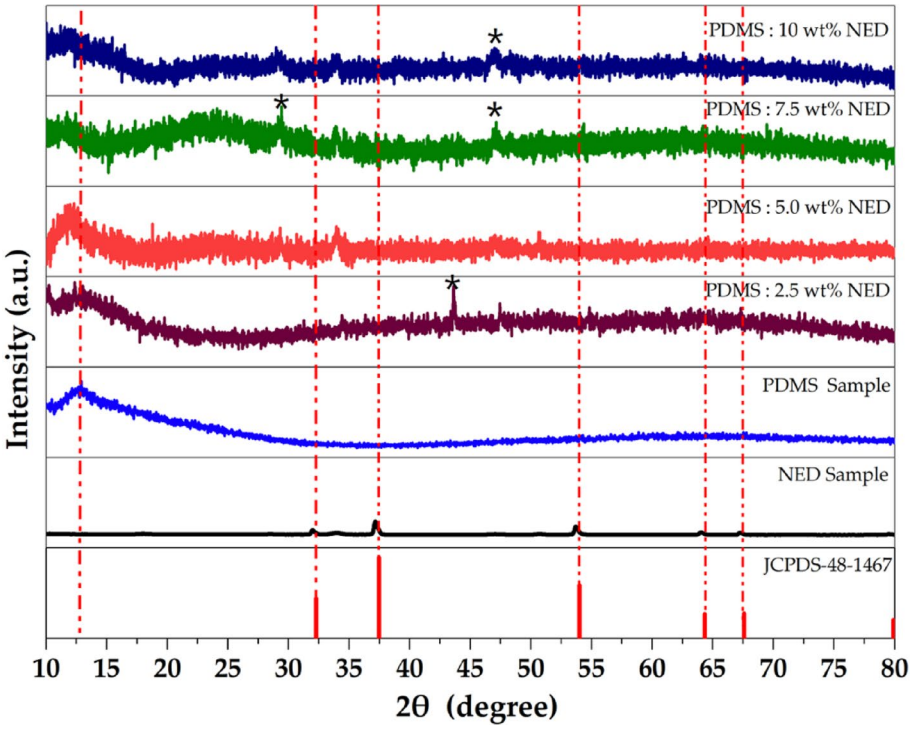

Fig. 5 XRD plots for NED, PDMS, PDMS: 2.5 wt.% NED, PDMS: 5 wt.% NED, PDMS: 7.5 wt.% NED, and PDMS: 10 wt.% NED sample

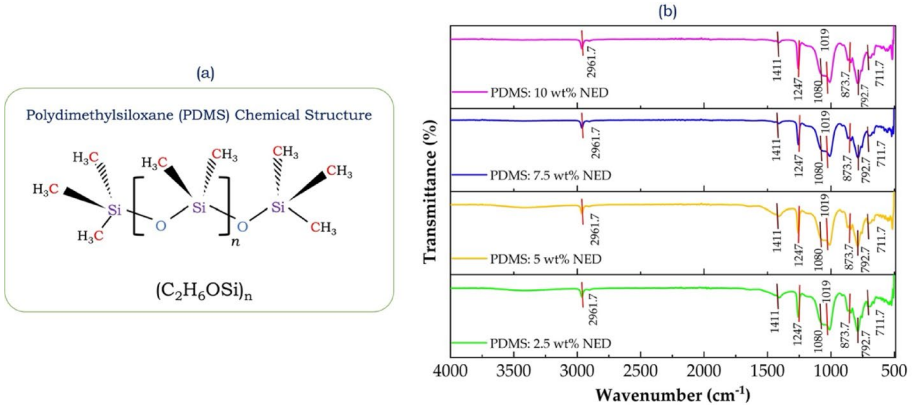

Fig. 6 FTIR plots for PDMS: 2.5 wt.% NED, PDMS: 5 wt.% NED, PDMS: 7.5 wt.% NED, and PDMS: 10 wt.% NED samples

successful film formation and curing. The prominent band at 2961.7 cm^{-1} is assigned to the C–H stretching vibration of the $–CH_3$ groups, while the band at 1411 cm^{-1} corresponds to $–CH_3$ bending. The peak at 1247 cm^{-1} is attributed to the Si–CH_3 vibration. The strong absorption bands at 1080 and 1019 cm^{-1} are associated with Si–O–Si stretching of the siloxane backbone. In addition, the band at 873.7 cm^{-1} is related to siloxane framework vibrations, the band at 792.7 cm^{-1} is assigned to the characteristic Si–CH_3 vibration of PDMS, commonly associated with CH_3 rocking coupled with Si–C stretching, and the feature at 711.7 cm^{-1} is attributed to related Si–C/CH_3 rocking vibrations [39, 40]. All composite compositions show nearly identical peak positions with only minor intensity variations, indicating that the incorporation of NED mainly results in

physical dispersion within the PDMS matrix without introducing new functional groups or causing significant chemical changes in the polymer network.

3.2 Diffuse reflectance spectroscopy (DRS)

The optical band gap (E_g) of the PDMS:NED composite films was determined from diffuse reflectance spectroscopy (RDS) data using the Kubelka–Munk (K–M) function in combination with the direct allowed Tauc relation, through the plot of $(F(R)h\nu)^2$ versus $h\nu$ (Fig. 7**).** The K–M function converts diffuse reflectance data into an absorption-equivalent form [41]. For optically thick samples, it is expressed as follows in Eq. (12):

$$F\left(R_\infty\right) = \frac{k}{s} = \left(\frac{1R}{2R}\right)^2 \tag{12}$$

where R is the absolute reflectance and $F(R_\infty)$ is directly proportional to the absorption coefficient k. The optical band gap was subsequently evaluated using the Tauc relation for direct allowed transitions. To estimate the band gap energy, the Tauc relation corresponding to direct allowed transitions was employed, as given in Eq. (13).

$$\left[F\left(R_\infty\right)h\nu\right]^2 \propto \left(h\nu - E_g\right) \tag{13}$$

Here, $h\nu$ is the photon energy. The linear portion of the Tauc plot is extrapolated to intersect the energy axis, and the intercept corresponds to the estimated band gap value. A well-defined linear region was observed near the absorption edge for all compositions, and the E_g was obtained by extrapolating the fitted linear segment to the energy axis. The extracted E_g values were 3.3305 ± 0.0136 eV (2.5 wt.% NED), 3.2692 ± 0.0082 eV (5 wt.% NED), 3.2890 ± 0.0059 eV (7.5 wt.% NED), and 3.268 ± 0.0068 eV (10 wt.% NED), with good linear fitting quality (R^2 = 0.914–0.982), supporting the suitability of the direct-transition model for the present composites. Overall, the films exhibit a wide optical

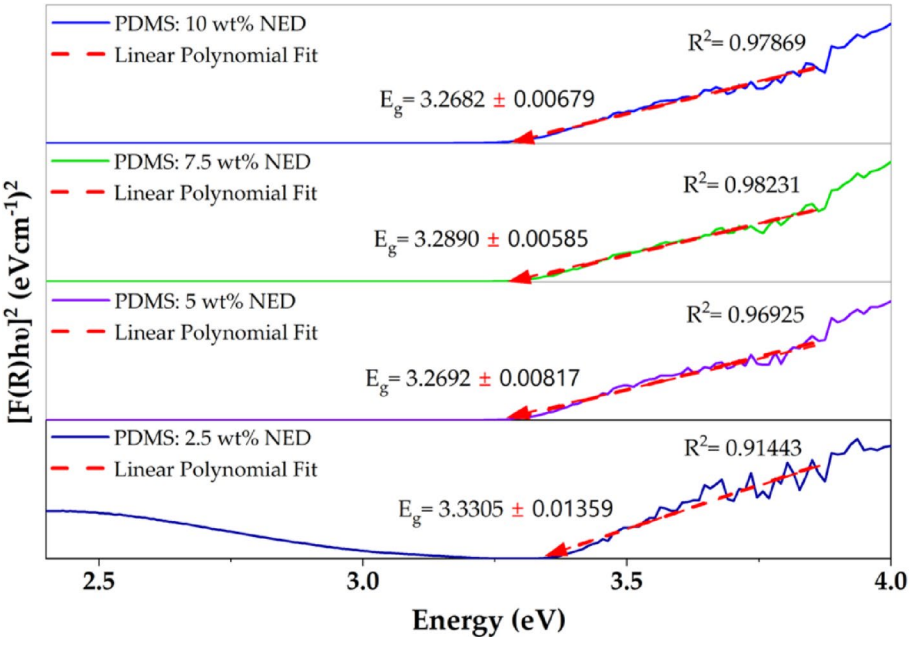

Fig. 7 Tauc's plots for PDMS: 2.5 wt.% NED, PDMS: 5 wt.% NED, PDMS: 7.5 wt.% NED, and PDMS: 10 wt.% NED samples

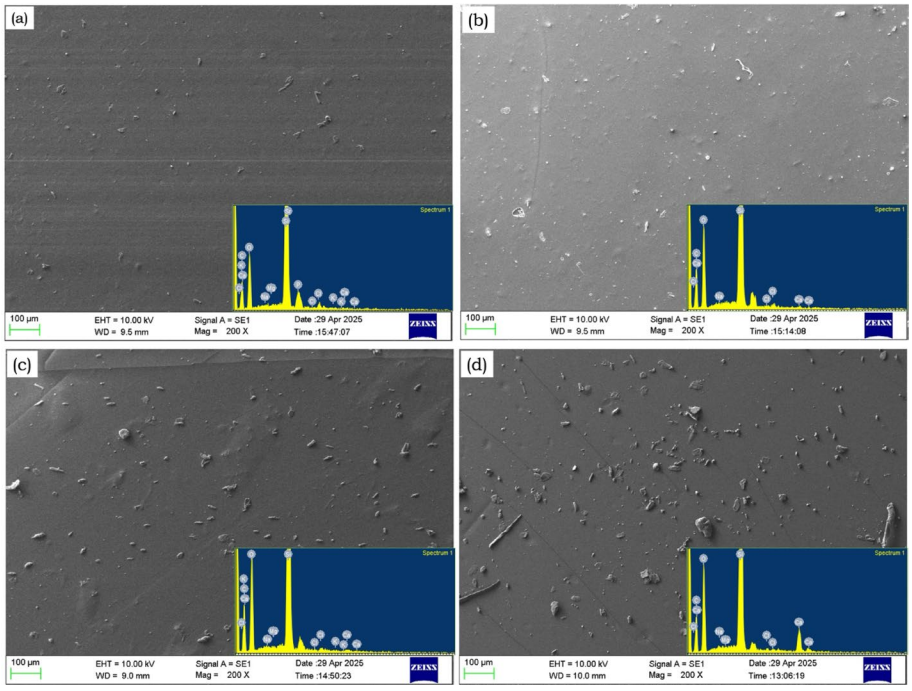

Fig. 8 SEM/EDS images for PDMS:NED composite at different wt. % of NED, **a** 2.5 wt. % of NED in PDMS, **b** 5 wt.% of NED in PDMS, **c** 7.5 wt.% of NED in PDMS, and **d** 10 wt.% of NED in PDMS

Table 1 Elemental composition of PDMS:NED composites

Sample names	Elemental composition (wt.%)			
	C	O	Si	Ca
PDMS: 2.5 wt.% NED	35.71	31.61	31.77	0.23
PDMS: 5 wt.% NED	33.73	29.75	35.91	0.32
PDMS: 7.5 wt.% NED	32.08	33.23	33.8	0.34
PDMS: 10 wt.% NED	29.92	33.76	31.45	0.44

band gap (~3.27–3.33 eV), confirming their dielectric nature. A slight reduction in E_g upon increasing NED loading (most evident from 2.5 wt.% to ≥ 5 wt.%) can be attributed to filler-induced interfacial interactions and localized tail states within the polymer matrix.

3.3 SEM and EDX analysis

From the SEM micrographs with EDS spectra in the inset of Fig. 8**,** it is observed that the PDMS matrix is continuous with dispersed particulate features of NED filler. As the filler content increases from 2.5 to 10 wt.%, it is observed that the surface of the composite becomes rougher and more particulate regions are observed. The 10 wt.% filler content shows the most intense agglomerate feature. This confirms that the filler is successfully dispersed in the PDMS matrix. The inset EDS spectra further confirm the presence of the major constituent elements C, O, Si, and Ca in all composite samples, and the corresponding quantitative elemental compositions are summarized in Table 1. Among these, C, O, and Si are associated with the PDMS matrix, whereas Ca originates from the incorporated NED filler. The measured Ca content shows an overall increasing trend with increasing NED loading, from 0.23 wt.% for PDMS: 2.5 wt.% NED to 0.44 wt.% for PDMS: 10 wt.% NED, confirming the successful incorporation of the filler phase into the

composites. In addition, minor quantities of K, Mg, Cl, and Na were also detected; however, these were present only in negligible amounts.

3.4 Impedance analysis

The Nyquist plot, characterized by a depressed semicircle, can be effectively modeled using an equivalent electrical circuit. This circuit consists of a constant phase element (CPE) and a resistor (R_b) arranged in parallel [42]. In this representation, CPE acts as a leaky capacitor. The complex impedance of a CPE consist both real and imaginary components and is typically described by, $Z_{\mathrm{CPE}} = \frac{1}{Q(j\omega)^n}$ where Q is the CPE constant, ω is the angular frequency, j is the imaginary unit, and n ($0 < n < 1$) characterizes the deviation from ideal capacitive behavior.

The real and imaginary parts of this impedance reflect the resistive and reactive contributions, respectively, and can be expressed analytically as shown in Eqs. (14) and (15) [43].

$$Z_r(\omega) = \frac{\cos\left(\frac{\pi p}{2}\right)}{k^{-1}\,\omega^p} \tag{14}$$

and

$$Z_i(\omega) = \frac{\sin\left(\frac{\pi p}{2}\right)}{k^{-1}\,\omega^p} \tag{15}$$

The expressions for the real and negative imaginary components of the complex impedance in a Nyquist plot—comprising a depressed semicircle formed by the parallel arrangement of R_b and CPE are provided in Eqs. (16) and (17) [44].

$$Z_r(\omega) = \frac{R_b + {R_b}^2 k_1^{-1}\omega^{p_1}\cos\left(\frac{\pi p_1}{2}\right)}{1 + 2R_b k_1^{-1}\omega^{p_1}\cos\left(\frac{\pi p_1}{2}\right) + {R_b}^2 k_1^{-2}\omega^{2p_1}} \tag{16}$$

$$Z_i(\omega) = \frac{{R_b}^2 k_1^{-1}\omega^{p_1}\sin\left(\frac{\pi p_1}{2}\right)}{1 + 2R_b k_1^{-1}\omega^{p_1}\cos\left(\frac{\pi p_1}{2}\right) + {R_b}^2 k_1^{-2}\omega^{2p_1}} \tag{17}$$

Here, k_1^{-1} represents the bulk geometrical capacitance of the NED. The parameter $p1$ denotes the angular ratio between the arc of the depressed semicircle and the full right angle (90°) defined by the real Z′ and imaginary Z″ axes.

The Nyquist spectra of the PDMS:NED composites in Fig. 9a show a single depressed semicircular arc with the center located below the real axis, evidencing a dominant bulk relaxation process with a distribution of relaxation times. Accordingly, the impedance response is well described by $R_b \parallel \mathrm{CPE}$ equivalent circuit, and the fitted curves closely overlap the experimental data for all compositions, confirming the adequacy of this model within the measured frequency window. With increasing NED loading, the arc progressively shifts toward lower Z' and Z" values up to 7.5 wt.% NED, indicating a reduction in bulk resistance and enhanced charge transport, consistent with improved interfacial pathways/percolative connectivity [45]. A slight shift back to higher impedance at 10 wt.% suggests the onset of microstructural limitations such as filler agglomeration and increased interfacial scattering, which can partially impede conduction despite higher filler content [46, 47]. No distinct low-frequency electrode polarization tail/

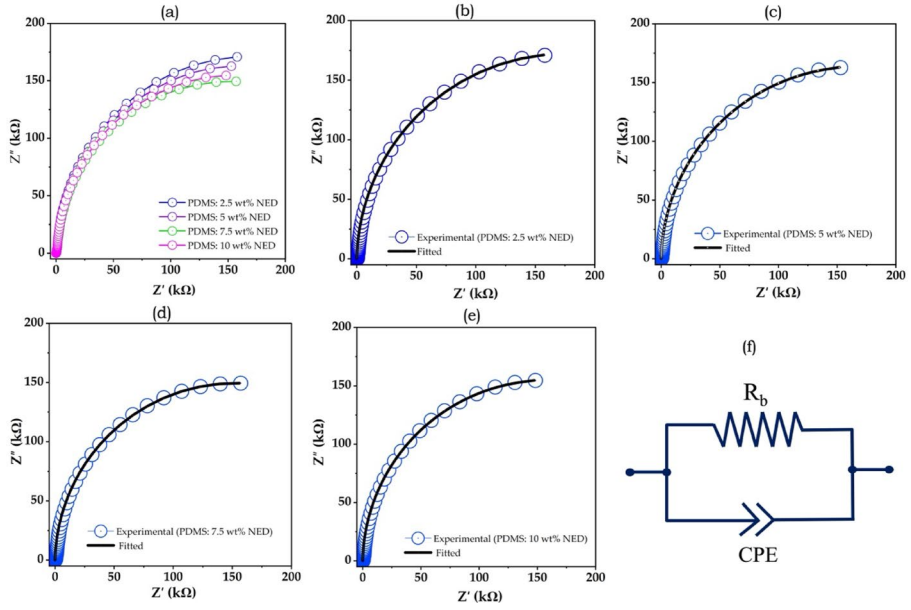

Fig. 9 Nyquist plots for **a** Different wt.% of PDMS: NED composites, fit curve of **b** PDMS: 2.5 wt.% NED, **c** PDMS: 5 wt.% NED, **d** PDMS: 7.5 wt.% NED, **e** PDMS: 10 wt.% NED, and **f** EEC circuit for fitting

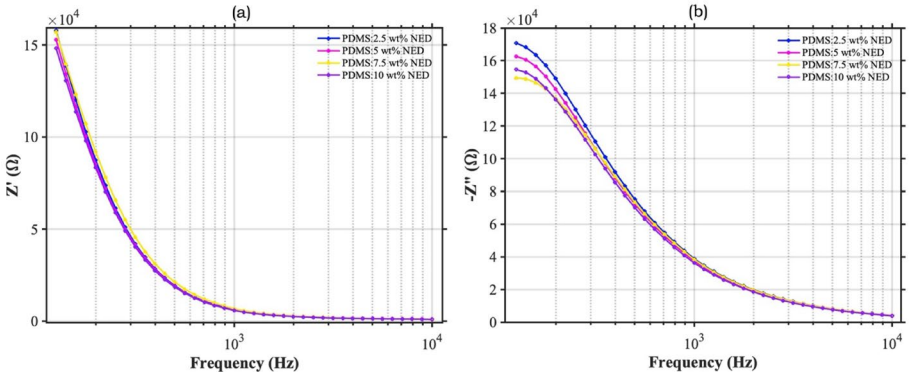

Fig. 10 Frequency domain impedance response **a** Real part of impedance vs. frequency, and **b** Imaginary part of impedance vs. frequency

second arc is resolved within the measured frequency window, and the extracted R_b values therefore reflect the intrinsic bulk response of the composites [48, 49]. Figure 9b–e shows the experimental values and fitted curves, and Fig. 9f shows the equivalent circuit adopted to fit the data. The fitted circuit shows a systematic change in transport with filler loading. The bulk resistance decreases from 350.989 kΩ (2.5 wt.%) to 304.957 kΩ (7.5 wt.%), corresponding to an increase in dc conductivity from 3.63×10^{-5} to 4.18×10^{-5} S/m, indicating enhanced charge transport due to improved interfacial pathways and filler-assisted conduction. A slight rise in R_b and reduction in σ_{dc} at 10 wt.% suggest the onset of microstructural effects such as filler agglomeration (Fig. 10).

3.5 Frequency-domain impedance response

In the range of measured frequency, it is observed that the magnitude of the real impedance (Fig. 10a) and the magnitude of the imaginary part of the impedance (Fig. 10b) decrease monotonically with all PDMS:NED loading fractions, consistent with a

response dominated by polarization, which becomes progressively bypassed at increasing values of ω and hence decreasing impedance [50]. Significantly, the -Z'' curves have a loading magnitude order in the low to mid-frequency range, with -Z'' having the highest magnitude at 2.5 wt.% NED, followed by 5 wt.% and 10 wt.%, and 7.5 wt.% having the lowest -Z'' magnitude of all. The decrease in -Z'' at a particular frequency implies a decrease in the material's reactive impedance, which in heterogeneous materials is associated with a decrease in the effective bulk resistive barrier and improvement in transport [51]. In this sense, the minimum -Z'' at 7.5 wt.% is consistent with the simultaneously reduced (Z') magnitude and the lower fitted bulk R_b, whereas the slight increase in -Z'' at 10 wt.% relative to 7.5 wt.% aligns with a modest recovery in R_b, possibly reflecting microstructural constraints rather than the emergence of a new relaxation. Notably, no distinct (-Z'') maximum is resolved in this window; for an ideal single-time-constant relaxation a peak in (-Z''(f)) is expected near a characteristic frequency, while the absence of a resolved maximum is typically associated with a characteristic process outside the probed band and/or a broadened, distributed (non-Debye) response that is routinely captured using constant-phase elements in equivalent-circuit descriptions. [52, 53].

3.6 AC conductivity

The frequency-dependent conductivity spectra display the characteristic two-regime response of polymer-based dielectric composites: a low-frequency plateau followed by a high-frequency dispersive rise (Fig. 11). The frequency-independent region at lower frequencies corresponds to the bulk dc conductivity governed primarily by the percolation of conductive pathways and consistent with the R_b values extracted from Nyquist fitting,

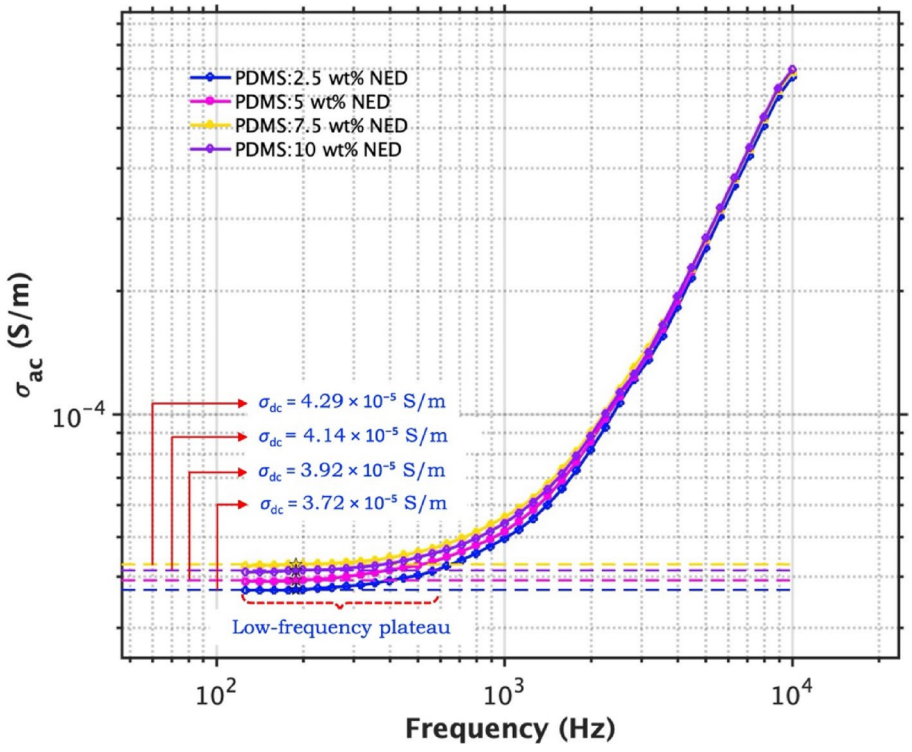

Fig. 11 AC conductivity response vs. frequency sweep

Table 2 Fitt values for bulk resistance, conductivity, and time constant

Sample	R_b (kΩ)	σ_{dc} (S/m) (from Eq. 11)	σ_{dc} (S/m) (from Fig. 10)
PDMS: 2.5 wt.% NED	350.989	3.62×10^{-5}	3.72×10^{-5}
PDMS: 5 wt.% NED	333.875	3.81×10^{-5}	3.92×10^{-5}
PDMS: 7.5 wt.% NED	304.957	4.18×10^{-5}	4.29×10^{-5}
PDMS: 10 wt.% NED	315.765	4.03×10^{-5}	4.14×10^{-5}

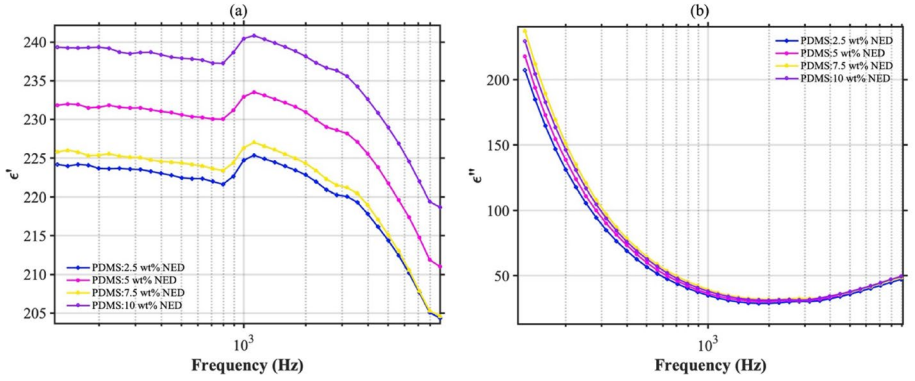

Fig. 12 Permittivity response vs. frequency sweep **a** Real part of permittivity, **b** imaginary part of permittivity

as shown in Table 2. Beyond the low frequency range, the σ_{ac} increases rapidly with frequency, indicating the onset of hopping/short-range charge transport and interfacial polarization effects typical of disordered heterogeneous systems; this behavior is commonly represented by Jonscher's power law [54] (Eq. 11).

3.7 Complex dielectric permittivity

The dielectric spectra show a clear frequency-dispersive response typical of heterogeneous polymer–filler systems. In Fig. 12a, the real permittivity $(\varepsilon\prime)$ remains high and weakly dependent on frequency in the low–mid frequency region, indicating interfacial/space-charge polarization (Maxwell–Wagner–Sillars contribution) arising from permittivity and conductivity mismatch between PDMS and NED [55],[56] With increasing frequency, $\varepsilon\prime$ decreases for all compositions due to the progressive inability of dipolar and interfacial charges to follow the rapidly alternating field; a subtle inflection around $\sim 10^3$ Hz suggests the onset of a relaxation process consistent with the bulk response seen in impedance fitting. In Fig. 12b, the imaginary permittivity (ε'') decreases markedly with frequency, reflecting diminishing conduction-related losses and reduced interfacial polarization losses at higher frequencies, followed by a slight upturn toward the highest frequencies that can be attributed to localized hopping/short-range carrier motion and measurement-domain dispersion. Across compositions, higher NED loading yields systematically large $\varepsilon\prime$ (and slightly elevated ε'' at low frequency), confirming that filler incorporation enhances polarization density; however, the similar curve shapes imply that the underlying relaxation/loss mechanism remains unchanged over the investigated loading range.

3.8 Dielectric loss

The dielectric loss tangent $(\tan\delta)$ spectra indicate a strong frequency dependence, a minimum, and a small increase at high frequency, indicating the onset of dipolar loss

mechanisms. At low frequency, high values of $\tan\delta$ can be attributed to the polarization of charges accumulated at the interface of the PDMS and NED (Maxwell–Wagner–Sillars polarization) as well as leakage currents, which decrease sharply as frequency increases. The charges accumulated at the interface cannot sustain the alternating electric field. In the mid-frequency range, close to the kHz region, all the compositions exhibit a similar value of $\tan\delta$ $(\sim 0.13 - 0.18)$, indicating a low level of dielectric loss, a more stable energy storage response, and a lower degree of polarization. A slight increase in $\tan\delta$ is observed as the frequency approaches 10^4 Hz, indicating the onset of localized carrier hopping. Among the compositions, the 7.5 wt.% NED composition exhibits a high value of $\tan\delta$ at low frequency, indicating a high level of polarization, possibly due to the better connectivity of the filler material (Fig. 13).

3.9 Complex electric modulus

The use of the electric modulus representation provides further insight into the relaxation processes. In this plot, electrode polarization effects are minimized. In Fig. 14a, the real part of the modulus (M') value increases with increasing frequency, eventually leveling off. This indicates a shift from a long-range charge migration process at lower frequencies to a process where the motion of charges is more and more restricted. In Fig. 14b, the imaginary modulus (M'') value decreases with increasing frequency and reaches a broad minimum at a kHz range. A small increase in M'' is then observed at higher frequencies. This indicates a complex relaxation process rather than a simple Debye process. This is consistent with the depressed semicircles obtained in the complex permittivity plot using $R_b \parallel$ CPE. The similarity in the modulus plots for the various compositions indicates a similar fundamental relaxation process with NED addition. The small differences in magnitude with increasing filler content may be related to changes in

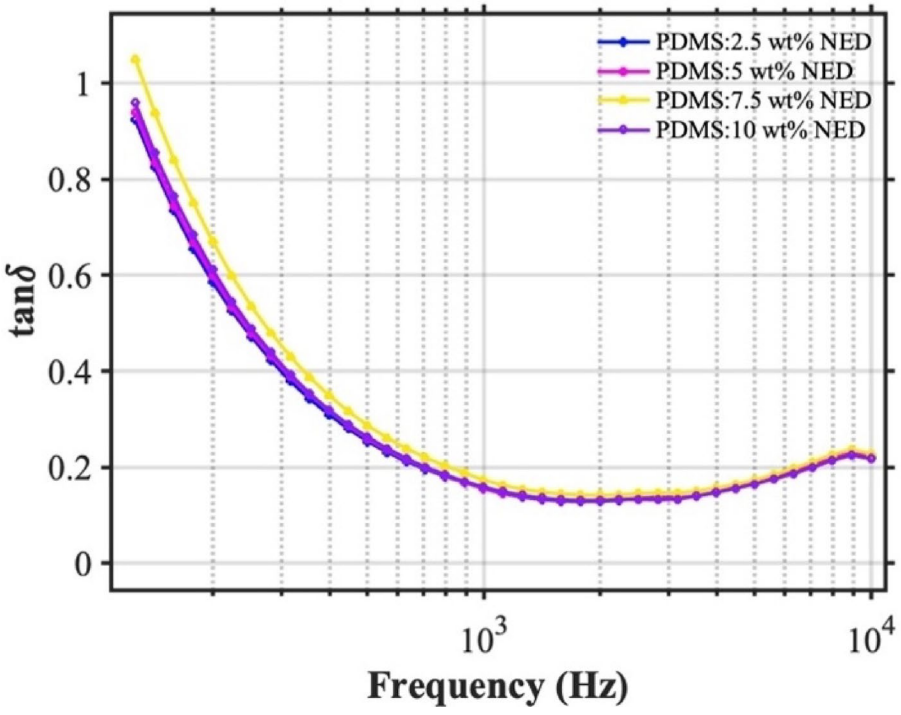

Fig. 13 Tangent loss response to sweep frequency

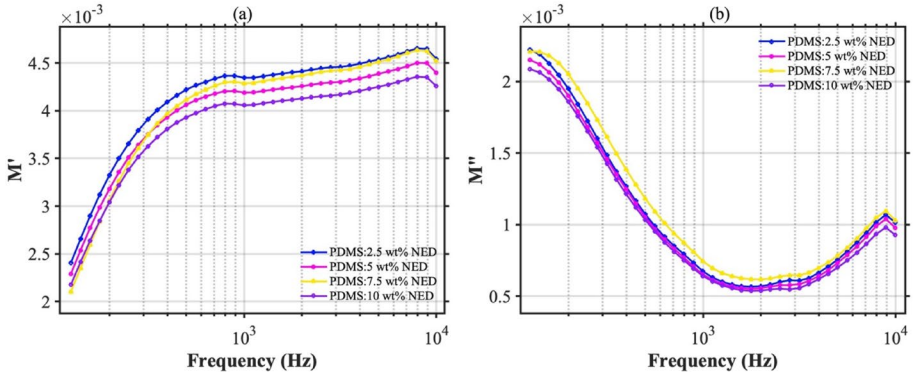

Fig. 14 Electric modulus of varied wt.% of PDMS: NED **a** Real part, and **b** Imaginary part Vs. frequency response

capacitance values with increasing filler content. The results indicate that the observed dielectric relaxation process is primarily bulk-controlled with a complex relaxation process, rather than electrode polarization within the measured frequency window.

4 Conclusion

This work presents a green and reproducible synthesis of PDMS:NED FCF, as well as a CaO-rich filler from biowaste influences the dielectric and impedance properties of a PDMS matrix. NED, a filler from cuttlefish bone, was prepared by calcination of cuttlefish bone at 750 °C, sonication, and lyophilization. The NED filler was mixed with PDMS by solution casting at a range of filler loadings (2.5–10 wt.%) and cured at RT to produce the FCF. Results from structural and chemical studies (XRD and FTIR) showed that the filler was successfully incorporated into the polymer matrix without any additional phases and without any chemical alteration of the polymer. The optical studies showed a large band gap of 3.27–3.33 eV, confirming the insulating properties of the composites. The morphology of the composites showed increased roughness and clustering of the filler, especially at 10 wt.%, consistent with the electrical properties. The impedance studies showed a $R_b \parallel$ CPE equivalent circuit. The bulk resistance decreases with filler loading up to 7.5 wt.% (enhanced transport) before showing a slight increase at 10 wt.%, identifying ~ 7.5 wt.% as the most favorable balance within this composition window. Dielectric analysis further reveals strong low-frequency interfacial polarization with relatively low and mid-frequency dielectric loss, which is advantageous for stable operation in flexible capacitive sensing regimes. Collectively, these results position the PDMS:NED system as a promising sustainable dielectric platform for flexible wearables, particularly for capacitive pressure sensors, and as a dielectric/tribolayer candidate, where permittivity tuning and interfacial polarization can be exploited to enhance device output in future device-level demonstrations.

Author contribution

Kiran Keshyagol: Conceptualization, Data curation, Formal analysis, Investigation, Methodology, Software, Validation, Visualization, Writing—original draft, Writing—review & editing; Shivashankarayya Hiremath: Conceptualization, Data curation, Formal analysis, Investigation, Methodology, Supervision, Validation, Visualization, Writing—review & editing; H.M. Vishwanatha: Data curation, Software, Supervision, Validation, Visualization, Writing—review & editing; Pavan Hiremath: Data curation, Software, Supervision, Validation, Visualization, Writing—review & editing; Tae-Won Kim: Supervision, Resources; Validation, Visualization, Writing—review & editing.

Funding

Open access funding provided by Manipal Academy of Higher Education, Manipal. This study did not receive any external funding.

Data availability
The authors confirm that the data supporting the findings of this study are available within the article.

Declarations

Ethics approval and consent to participate
Not applicable.

Consent to publication
All authors have read and approved the manuscript and consent to its publication.

Competing interests
The authors declare no competing interests.

Received: 11 February 2026 / Accepted: 19 May 2026
Published online: 23 May 2026

References

1. Senthil Kumar K, Chen P-Y, Ren H. A review of printable flexible and stretchable tactile sensors. Research. 2019. https://doi.org/10.34133/2019/3018568.
2. Xie M, et al. Flexible multifunctional sensors for wearable and robotic applications. Adv Mater Technol. 2019. https://doi.org/10.1002/admt.201800626.
3. Thirmal C, Mohan PN, Suresh G, Raju KCJ, Vishwam T. Improved dielectric and AC conductivity properties of P(VDF-TrFE)-Nafion blends for high-temperature flexible capacitor applications. Curr Appl Phys. 2022;44:63–70. https://doi.org/10.1016/j.cap.2022.09.010.
4. Thirmal C, Nayek C, Murugavel P, Subramanian V. Magnetic, dielectric and magnetodielectric properties of PVDF-La0.7Sr0.3MnO3 polymer nanocomposite film. AIP Adv. 2013. https://doi.org/10.1063/1.4830282.
5. Dong C, et al. Flexible capacitive pressure sensor: material, structure, fabrication and application. Nondestruct Test Eval. 2024;39(7):1749–90. https://doi.org/10.1080/10589759.2024.2327639.
6. Mathew S, Chintagumpala K. A review of recent progress in flexible capacitance pressure sensors: materials design, printing methods, and applications. Adv Compos Hybrid Mater. 2025;8(3):236. https://doi.org/10.1007/s42114-025-01304-2.
7. Udofa ES, Mohamed Ali MS, Leow PL. Recent development in triboelectric nanogenerators: a review. J Mater Sci Mater Electron. 2026;37(1):6. https://doi.org/10.1007/s10854-025-16223-7.
8. Rajasekar M, Sivakumar M. Recent trends and future perspectives of triboelectric nanogenerators (TENGs) and applications. RSC Adv. 2025;15(57):49600–42. https://doi.org/10.1039/D5RA06645J.
9. Duan Z, Cai F, Chen Y, Chen T, Lu P. Advanced applications of porous materials in triboelectric nanogenerator self-powered sensors. Sensors. 2024;24(12):3812. https://doi.org/10.3390/s24123812.
10. Papaefstathiou M, Elgendi M, Menon C. Balancing sensitivity and integration in capacitive pressure sensors for textile-based health monitoring. npj Biosensing. 2025;2(1):40. https://doi.org/10.1038/s44328-025-00059-6.
11. Ntostoglou E, et al. Understanding the interactions between biowaste valorisation and the Sustainable Development Goals: insights from an early transition stage. Int J Urban Sustain Dev. 2024;16(1):53–72. https://doi.org/10.1080/19463138.2024.2319795.
12. Huan X, et al. Multi-stimuli-responsive dielectric composites: composition–structure–nanoscale mechanism–function framework for dynamic dielectric engineering. Adv Funct Mater. 2025. https://doi.org/10.1002/adfm.202521845.
13. Li X, et al. High-resolution liquid metal–based stretchable electronics enabled by colloidal self-assembly and microtransfer printing. Sci Adv. 2025. https://doi.org/10.1126/sciadv.adw3044.
14. Song Y, Gao X, Zheng M, Hou Y. Flexible, highly out-of-plane thermal conductive and electrically insulating multi-scale oriented BNNS/PDMS thermal interface materials. J Alloys Compd. 2025;1041:183850. https://doi.org/10.1016/j.jallcom.2025.183850.
15. Pu J, et al. Dual-dielectric-layer-based iontronic pressure sensor coupling ultrahigh sensitivity and wide-range detection for temperature/pressure dual-mode sensing. Adv Mater. 2025. https://doi.org/10.1002/adma.202503926.
16. Rerngroen N, Sasipongpan A, Vittayakorn W. Synergistic enhancement of mechanical and dielectric properties in BaTiO3/PDMS composites for flexible energy harvesting devices. Polym-Plast Technol Mater. 2026;65(1):160–76. https://doi.org/10.1080/25740881.2025.2586689.
17. Wang B, et al. Fabrication and performance study of triboelectric nanogenerators based on PDMS@TiO2 nanocomposite films. J Phys Conf Ser. 2026;3175(1):012082. https://doi.org/10.1088/1742-6596/3175/1/012082.
18. Mathew S, Chintagumpala K. A highly sensitive capacitance pressure sensor with ZnO-GO-PVDF dielectric composite layer for wearable applications. J Appl Polym Sci. 2026. https://doi.org/10.1002/app.70439.
19. Gao Y, et al. Improved electro-actuation property of dielectric elastomer composites regulated by one-dimensional $CaCu_3Ti_4O_{12}$@TiO_2 core–shell construction. J Appl Polym Sci. 2024. https://doi.org/10.1002/app.55379.
20. Kanwal A, et al. A comprehensive review of piezoelectric $BaTiO_3$-based polymer composites for smart tactile sensing. Emergent Mater. 2025;8(8):6137–76. https://doi.org/10.1007/s42247-025-01208-3.
21. Rafiefard N, et al. High-performance flexible and stretchable self-powered surface engineered PDMS-TiO_2 nanocomposite based humidity sensors driven by triboelectric nanogenerator with full sensing range. Sens Actuators B Chem. 2023;378:133105. https://doi.org/10.1016/j.snb.2022.133105.
22. Mathew S, Chintagumpala K. Design and characterization of PDMS-CB-ZnO-ternary composite based flexible capacitance pressure sensors for wearable applications. Flex Print Electron. 2025;10(2):025004. https://doi.org/10.1088/2058-8585/adc81e.
23. Zhang Y-B, et al. Hybrid electrode-architecture engineering of $CaCu_3Ti_4O_{12}$ humidity sensors: design, performance evaluation, and simulation validation. Ceram Int. 2026. https://doi.org/10.1016/j.ceramint.2026.01.460.

24. Karmakar S, et al. Origin of giant dielectric permittivity and localized polaron-supported electrical conduction in $CaCu_3Ti_4O_{12}$ for extreme environment energy storage applications. Sci Rep. 2026;16(1):6994. https://doi.org/10.1038/s41598-026-36234-6.
25. Thorali N, Kim DS, Lee H, Kim DR, Lee D-W. Enhancing sensitivity in wireless capacitive pressure sensors via highly flexible LC circuits utilizing porous polydimethylsiloxane dielectric layer. Sens Actuators A Phys. 2024;379:115973. https://doi.org/10.1016/j.sna.2024.115973.
26. Wang X, Zhang Y, Zhang T, Fu G, Zhu Y, Liu Y. Modeling and relative permittivity modulation of Cu/PDMS capacitive flexible sensor for pressure sensing. Sensors Basel. 2025;25(3):637. https://doi.org/10.3390/s25030637.
27. Zhang L, Jing R, Zhang S, Jin L. Multiscale microstructure design for high-performance dielectric energy storage materials. Microstructures. 2026. https://doi.org/10.20517/microstructures.2025.89.
28. Lv J, et al. Micro–nano surface engineering and property modulation: insights from black silicon for advanced material applications. Chem Soc Rev. 2026. https://doi.org/10.1039/D5CS01448D.
29. Lee K, Park S, Jung K, Moon IY, Ryu JH, Kim KM. Enhanced performance of polydimethylsiloxane-based triboelectric nanogenerator using $BaTiO_3$/MWCNTs. J Cryst Growth. 2025;649:127952. https://doi.org/10.1016/j.jcrysgro.2024.127952.
30. Piras S, et al. Biomimetic use of food-waste sources of calcium carbonate and phosphate for sustainable materials—a review. Materials Basel. 2024;17(4):843. https://doi.org/10.3390/ma17040843.
31. Ooi HK, et al. Progress on modified Calcium Oxide derived waste-shell catalysts for biodiesel production. Catalysts. 2021;11(2):194. https://doi.org/10.3390/catal11020194.
32. Zulkarnain NA, Ramli A, Kadir NHA. Optimization on characterization and physicochemical of non-calcined and calcined nanocrystallite of cuttlefish (*Sepia officinalis*) bones powder for sustainable green technology applications. Biointerface Res Appl Chem. 2024;14(3):58. https://doi.org/10.33263/BRIAC143.058.
33. Periasamy K, Mohankumar G. Sea coral-derived cuttlebone reinforced epoxy composites: characterization and tensile properties evaluation with mathematical models. J Compos Mater. 2016;50(6):807–23. https://doi.org/10.1177/0021998315581512.
34. Keshyagol K, Hiremath S, Vishwanatha HM, Hiremath P. Sustainable dielectric materials for energy storage: processing, properties, and performance evaluation. Mater Today Sustain. 2025;21:101281. https://doi.org/10.1016/j.mtsust.2025.101281.
35. Abdullah RM. Investigation of ion transport in plasticized polymer electrolytes using electrical equivalent circuit (EEC) modeling. J Mater Sci Mater Electron. 2024. https://doi.org/10.1007/s10854-024-12564-x.
36. Migahed MD, Ishra M, Fahmy T, Barakat A. Electric modulus and AC conductivity studies in conducting PPy composite films at low temperature. J Phys Chem Solids. 2004;65(6):1121–5. https://doi.org/10.1016/j.jpcs.2003.11.039.
37. Bhadra S, Singha NK, Khastgir D. Dielectric properties and EMI shielding efficiency of polyaniline and ethylene 1-octene based semi-conducting composites. Curr Appl Phys. 2009;9(2):396–403. https://doi.org/10.1016/j.cap.2008.03.009.
38. Abdulkareem SS. Structural, morphological and electrical properties of chitosan/methylcellulose blend polymer doped with different concentrations of NH_4NO_3. Mater Res Express. 2021;8(8):086301. https://doi.org/10.1088/2053-1591/ac1d69.
39. Aziz SB, Hamsan MH, Brza MA, Kadir MFZ, Muzakir SK, Abdulwahid RT. Effect of glycerol on EDLC characteristics of chitosan:methylcellulose polymer blend electrolytes. J Mater Res Technol. 2020;9(4):8355–66. https://doi.org/10.1016/j.jmrt.2020.05.114.
40. Rezakazemi M, Vatani A, Mohammadi T. Synergistic interactions between POSS and fumed silica and their effect on the properties of crosslinked PDMS nanocomposite membranes. RSC Adv. 2015;5(100):82460–70. https://doi.org/10.1039/C5RA13609A.
41. Zhang J, et al. Study on preparation and anticorrosive performance of a new high hydrophobic anticorrosive coating. J Appl Polym Sci. 2023. https://doi.org/10.1002/app.53459.
42. Kim D, Lee JH, Hwang I-C, Chung I. Enabling room-temperature phosphorescence via solvent-mediated crystal packing in 1,8-naphthalimide hybrid perovskites. J Solid State Chem. 2026;356:125828. https://doi.org/10.1016/j.jssc.2026.125828.
43. A. Shukur D, Aziz BK, Aziz SB. FTIR, XRD electrical and dielectric characteristics of solid polymer blend electrolytes based on chitosan: dextran inserted with $NH4CF_3SO_3$ salt as proton provider. Int J Polym Anal Characterization. 2026; https://doi.org/10.1080/1023666X.2025.2603959
44. Bouragba FZ, Assekouri A, Elhatimi W, Moujahid EM, Sabbar E. Decreasing dielectric loss of CoAl-LDH by polymerization of intercalated monomer at organic-inorganic interface. Synth Met. 2026;317:118080. https://doi.org/10.1016/j.synthmet.2026.118080.
45. Arof AK, Amirudin S, Yusof SZ, Noor IM. A method based on impedance spectroscopy to determine transport properties of polymer electrolytes. Phys Chem Chem Phys. 2014;16(5):1856–67. https://doi.org/10.1039/C3CP53830C.
46. Kirkpatrick S. Percolation and conduction. Rev Mod Phys. 1973;45(4):574–88. https://doi.org/10.1103/RevModPhys.45.574.
47. Atif R, Inam F. Reasons and remedies for the agglomeration of multilayered graphene and carbon nanotubes in polymers. Beilstein J Nanotechnol. 2016;7:1174–96. https://doi.org/10.3762/bjnano.7.109.
48. Arjmandi SK, Yeganeh JK, Zare Y, Rhee KY. Development of Kovacs model for electrical conductivity of carbon nanofiber–polymer systems. Sci Rep. 2023;13(1):7. https://doi.org/10.1038/s41598-022-26139-5.
49. Zhang L, et al. Recent advances in electrochemical impedance spectroscopy for solid-state batteries. Energy Storage Mater. 2024;69:103378. https://doi.org/10.1016/j.ensm.2024.103378.
50. Barsoukov E, Macdonald RJ. Impedance spectroscopy theory, experiment, and applications. Impedance Spectrosc. 2005. https://doi.org/10.1002/0471716243.fmatter.
51. Barsoukov E, Macdonald JR, editors. Impedance spectroscopy. Wiley; 2005. https://doi.org/10.1002/0471716243.
52. Lasia A. Electrochemical impedance spectroscopy and its applications. New York: Springer New York; 2014. https://doi.org/10.1007/978-1-4614-8933-7.
53. Lazanas AC, Prodromidis MI. Electrochemical impedance spectroscopy—a tutorial. ACS Meas Sci Au. 2023;3(3):162–93. https://doi.org/10.1021/acsmeasuresciau.2c00070.
54. Balaguera EH. A full capacitive picture of the constant phase element: estimations from impedance spectroscopy, distribution of relaxation times and fractional calculus. Electrochem Commun. 2025;180:108053. https://doi.org/10.1016/j.elecom.2025.108053.
55. Jonscher AK. The 'universal' dielectric response. Nature. 1977;267(5613):673–9. https://doi.org/10.1038/267673a0.

56. Althumairi NA, Hjiri M, Aldukhayel AM, Jbeli A, Nassar KI. Recent advances in dielectric and ferroelectric behavior of ceramic nanocomposites: structure property relationships and processing strategies. Nanomaterials. 2025;15(17):1329. https://doi.org/10.3390/nano15171329.

Publisher's Note

Springer Nature remains neutral with regard to jurisdictional claims in published maps and institutional affiliations.